Periodic confined cell migration drives partially reversible chromatin reorganization in cancer cell lines

Maria del Valle Blazquez-Romero[1,2,3], Marco Mendivil-Carboni[4,5], Maria Sarasquete-Martinez[3], Alejandro Sainz-Agost[6,7], Fernando Falo[6,7], Marco De Corato[1,3*], Maria Jose Gomez-Benito[2,3*]

[1] Department of Science and Technology of Materials and Fluids, Fluid Dynamics Technology Group (TFD), Universidad de Zaragoza, Zaragoza, Spain.

[2] Department of Mechanical Engineering, Multiscale in Mechanical and Biological Engineering (M2BE), Universidad de Zaragoza, Zaragoza, Spain.

[3] Aragon Institute of Engineering Research (I3A), Zaragoza, Spain.

[4] Department of Structure of Matter, Thermal Physics and Electronics, Universidad Complutense de Madrid, Madrid, Spain.

[5] Interdisciplinary Group on Complex Systems (GISC), Universidad Complutense de Madrid, Madrid, Spain.

[6] Department of Condensed Matter Physics, Universidad de Zaragoza, Zaragoza, Spain.

[7] Institute for Biocomputation and Physics of Complex Systems (BIFI), Universidad de Zaragoza, Zaragoza, Spain.

[*] Corresponding authors. E-mails: mdecorato@unizar.es, gomezmj@unizar.es

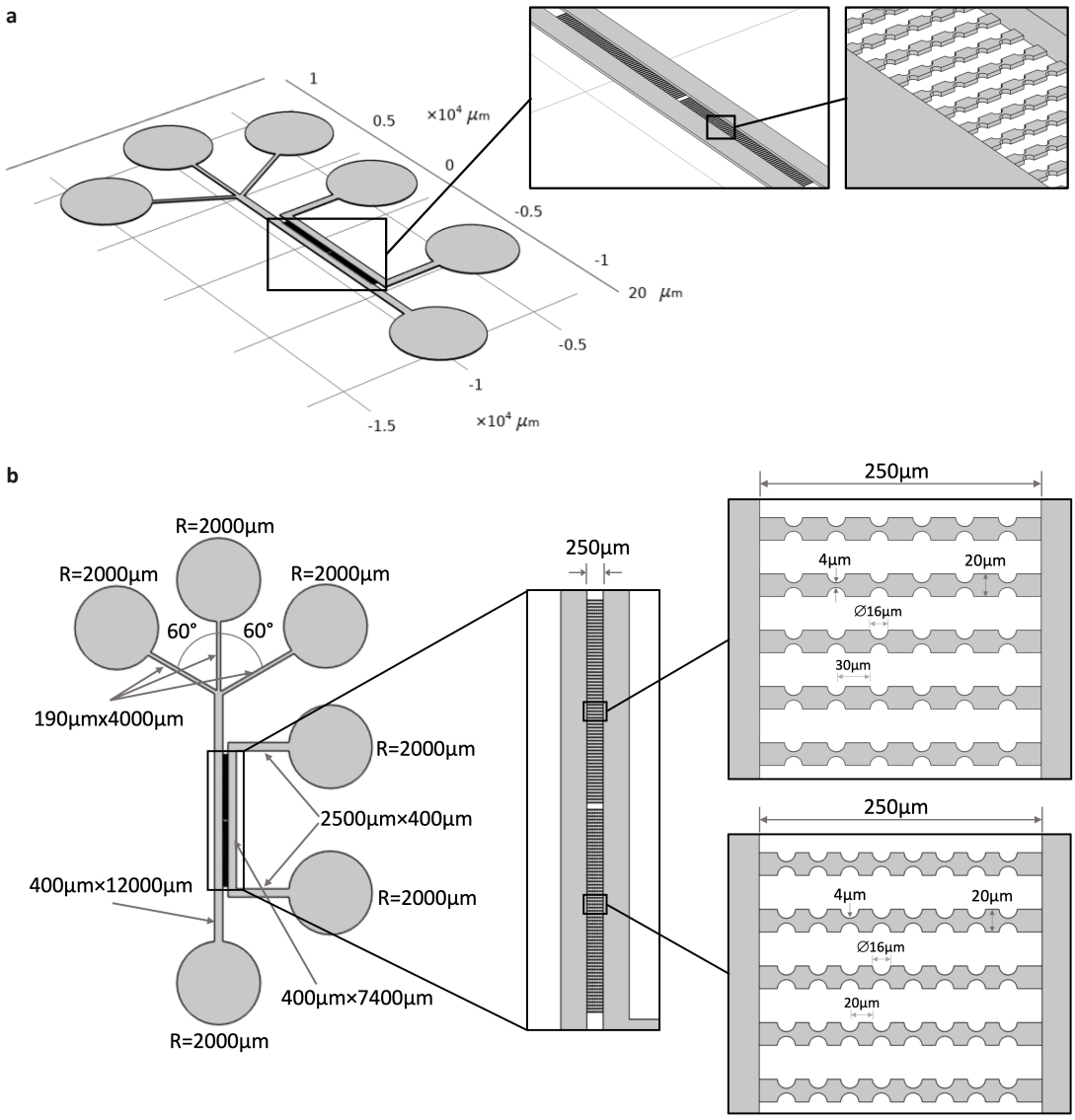

Supplementary Figure 1 Comprehensive overview of our microfluidic device. a Three-dimensional view of the microfluidic device and zoomed regions to show the confining microchannel array. **b** Dimensional details for our microfluidic device design, long channels (right top) and short channels (right bottom).

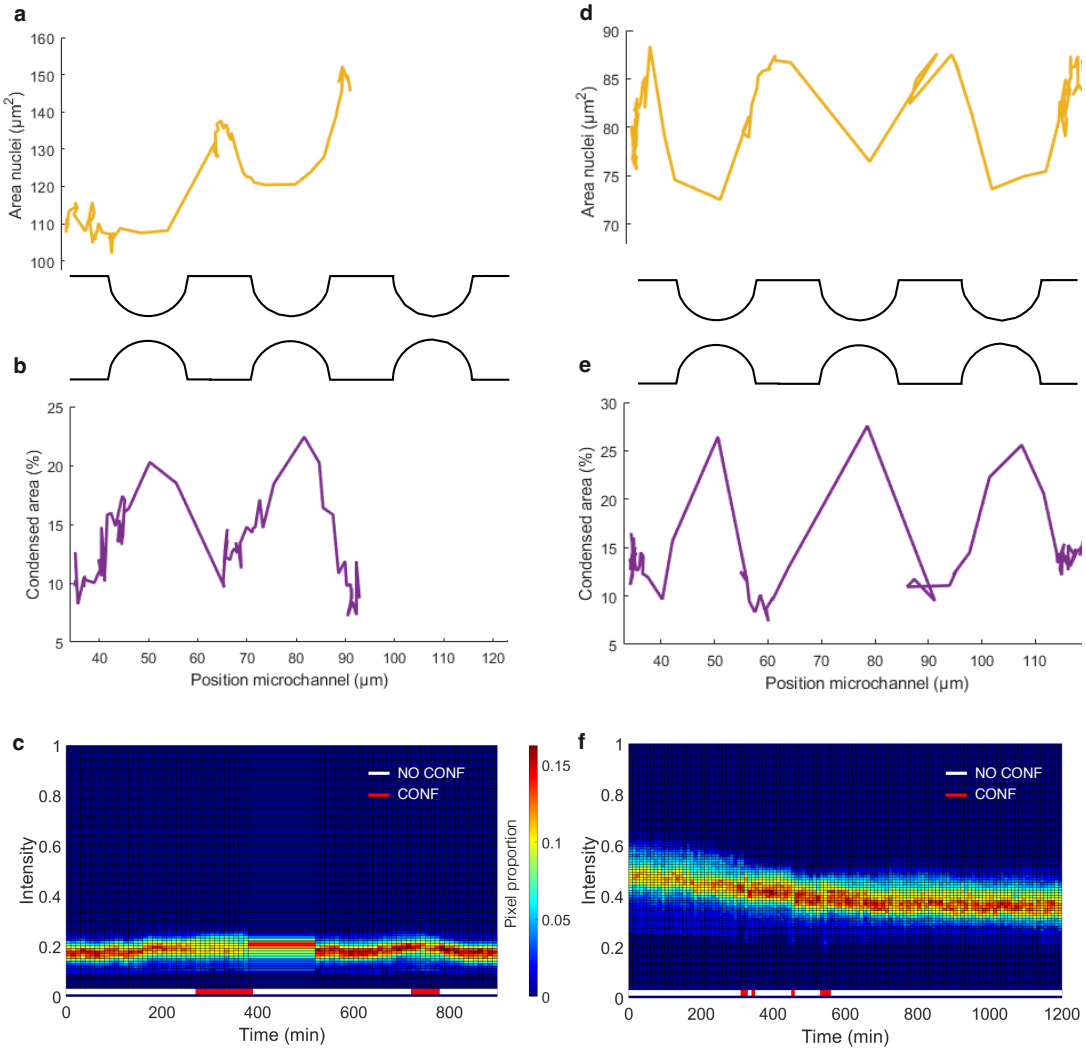

Supplementary Figure 2 Single-cell analysis for PACA-H2B-GFP cells during migration through periodic confinements in microfluidic devices. a Typical results for a slow migration cell (PACA-H2B-GFP cell line) representing the evolution of the area of the nucleus with respect to the distance traveled within the channel, **b** the relative area for the segmented highly-condensed chromatin regions, i.e. the percentage of nucleus area identified as highly-condensed, with respect to the distance traveled within the channel and **c** the evolution of the fluorescence intensity profile of the nucleus against time. **d-f** Similarly, typical results for a fast migrating cell (PACA-H2B-GFP cell line).

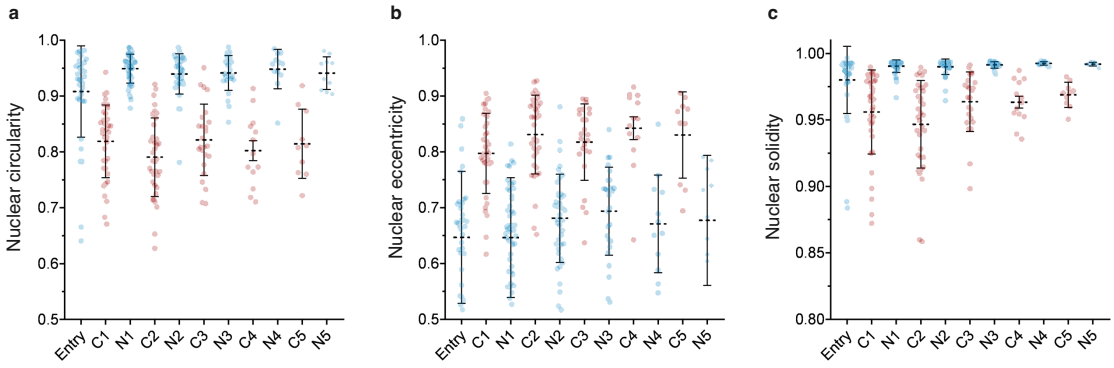

Supplementary Figure 3 Assessment of nuclear morphology a Cell population analysis for nuclear circularity, **b** nuclear eccentricity and **c** nuclear solidity among PACA-H2B-GFP cells migrating through short microchannels (n=65). Note that non-confining regions are colored in blue and confinements are in red. These nuclear morphological parameters suggests that nuclei in non-confining regions are characterized by a smooth regular rounded shape. As expected, nuclei elongate during confinement since they exhibit a significantly larger eccentricity. Despite the decrease in solidity for confined nuclei, the minimum value reported is well above those observed in concave, fragmented or protrusive nuclei. These results support that the analysis was conducted on structurally intact and morphologically regular nuclei. Bars show mean ± standard deviation.

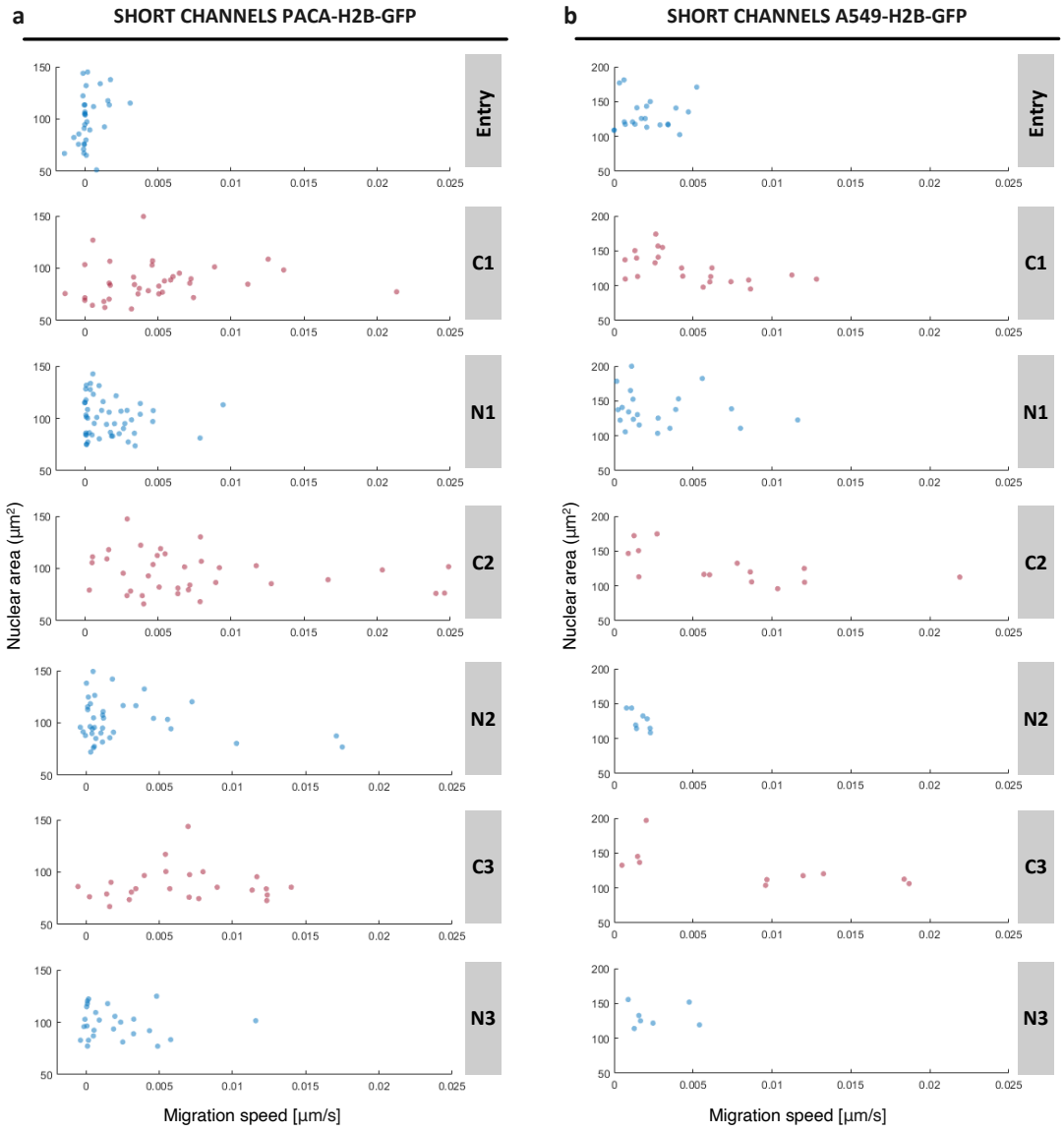

Supplementary Figure 4 Correlation for migration speed and nuclear area a Cell population analysis for the correlation of migration speed (x-axis) and nuclear area (y-axis) in PACA-H2B-GFP cells (n=65). Each data point is defined by mean speed and mean nuclear area for an individual nucleus within the specific region indicated on the right. Note that results for non-confining regions are colored in blue while results for confining regions are colored in red. **b** Similarly, cell population analysis for the correlation of migration speed and nuclear area in A549-H2B-GFP cells (n=42). Migration during confinement is frequently characterized by a wider distribution towards higher speeds, often corresponding to cells with smaller nuclear areas.

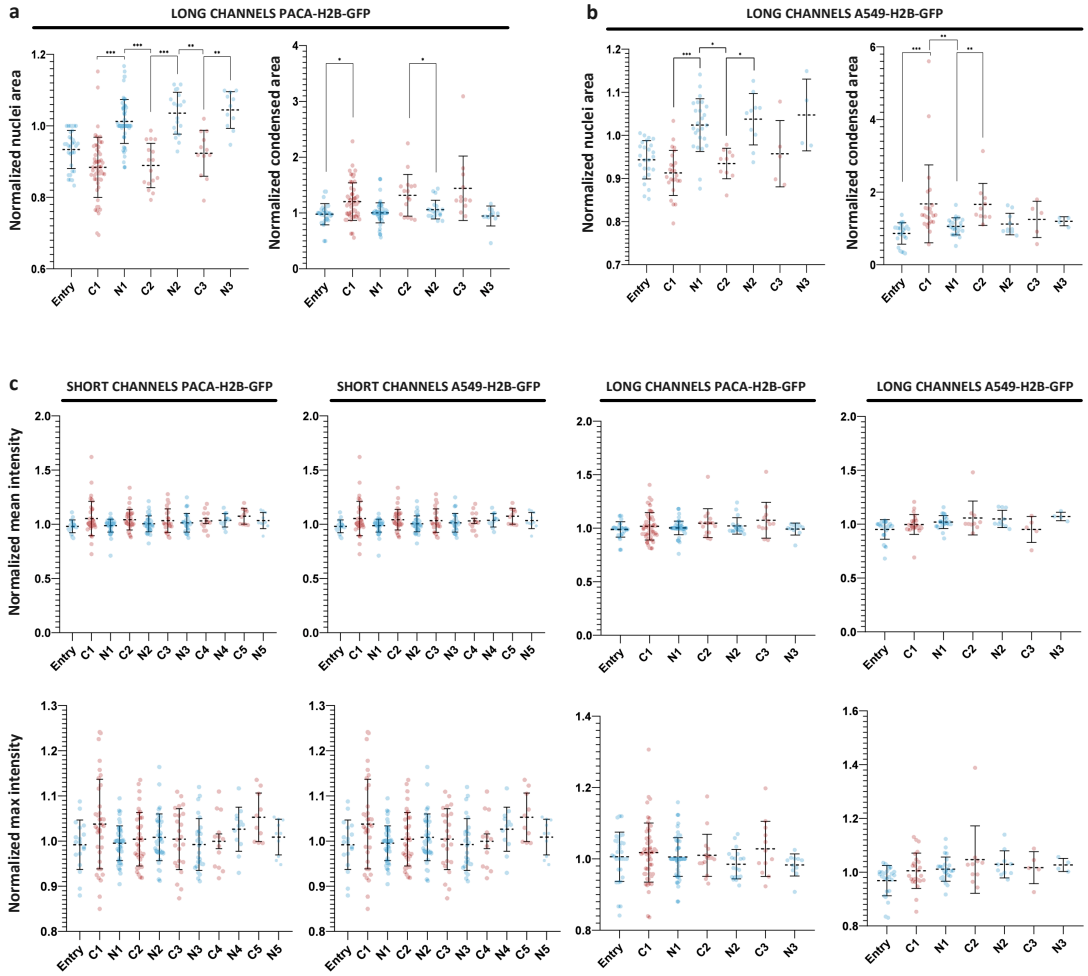

Supplementary Figure 5 Supplementary quantification for the cell population analysis. Each data point in a column corresponds to a single cell and represents the average among every frame in which the geometric center of the cell lies within the specified microchannel region, where C1-C5 represent the successive confining regions and N1-N5 represent the non-confining regions following the entry. Note that the results for the confinements are colored red whereas those for unconfined cells are in blue. **a** Left: Evolution of the normalized nuclei area for PACA-H2B-GFP cells migrating through long channels shows a significant reversible decrease upon the deformation through a confinement and a global growing trend over time. Right: Evolution of the normalized highly-condensed chromatin area for PACA-H2B-GFP cells migrating through long-channels depicts a strong increase in confining regions and a recovery to the basal highly-condensed area for non-confining regions (n=71). **b** Similarly, distributions for normalized nuclei area (left) and normalized highly-condensed chromatin area (right) of A549-H2B-GFP cells (n=26), which consistently reveal an analogous pattern to PACA-H2B-GFP cells. **c** Evolutions of the normalized mean intensity (top) and the normalized maximum intensity (bottom) for PACA-H2B-GFP and A549-H2B-GFP migrating through both long and short channels. The statistical analysis revealed no significant differences for these intensity values and a great variability, particularly for the maximum intensity distributions. Bars show mean ± standard deviation. Kruskal-Wallis test with Dunn's post hoc test for multiple comparisons was performed, p-value: $p<0.05$ (*), $p<0.01$ (**), $p<0.001$ (***).

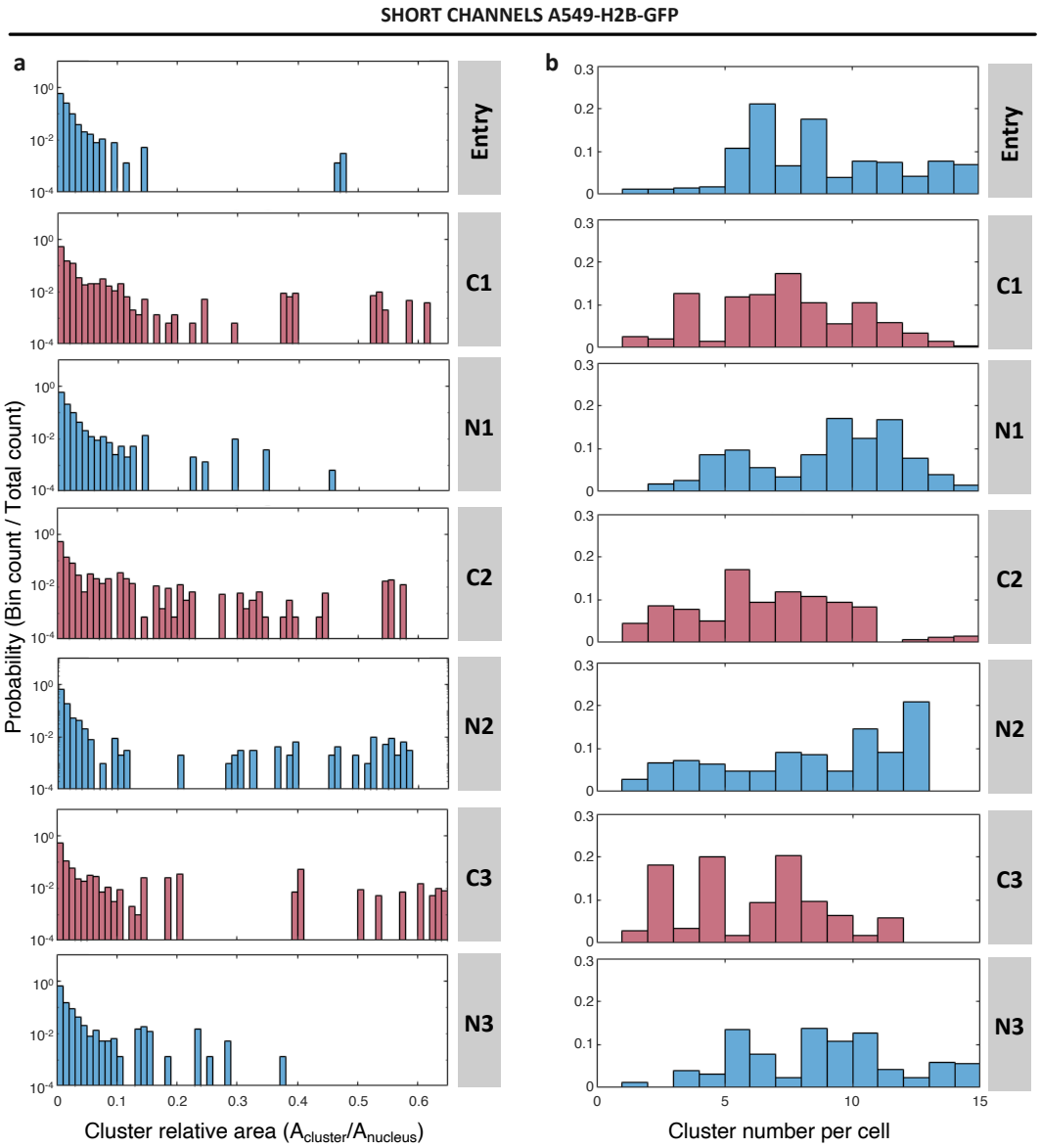

Supplementary Figure 6 Distributions for the size and number of condensed chromatin clusters in A549-H2B-GFP cells migrating through short channels. a Histograms to estimate the evolution of the size distribution for individual highly-condensed chromatin clusters in A549-H2B-GFP cells (n=42). Histograms represent the normalized count (bin count over the total number of counts) for the relative area of individual highly-condensed chromatin areas, i.e., the area for each highly-condensed segmented region ($A_{cluster}$) over the total area of its nucleus ($A_{nucleus}$). From top to bottom, each graph corresponds to a different microchannel region, either non-confining (in red) or confining (in blue), and contains the relative area for every cluster in each nucleus during all frames in which the nucleus lies within the corresponding region. The counts for the condensed chromatin clusters in each cell are normalized to 100 data points to avoid misrepresenting cells that migrate faster through the microchannels. **b** Similarly, histograms to estimate the evolution of the distribution for the number of chromatin clusters per cell (n=42).

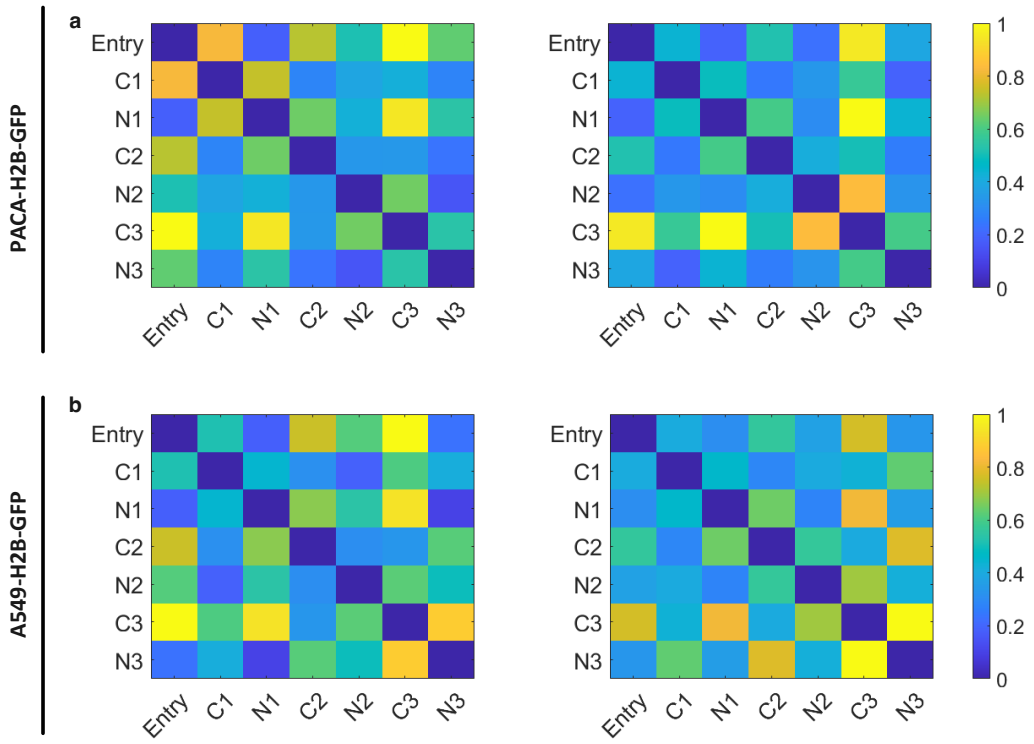

Supplementary Figure 7 Results for the quantification using Wasserstein distance. a Heatmaps for the Wasserstein distances of the pairwise comparison of chromatin cluster size distributions (left) and cluster number per cell distributions (right) for PACA-H2B-GFP cells (in Figure 4). Wasserstein distances represent how similar two distributions are such that smaller distance values correspond to more resembling distributions. Wasserstein distances are normalized relative to the maximum value in each heatmap. Note that shorter distances support how similar the distributions are among confinements and among non-confining regions. Interestingly, the Wasserstein distance for every confinement paired with a non-confining region decreases notably as the non-confining region locates further downstream the microchannel in both, cluster size and cluster number analysis. **b** Similarly, heatmaps for the Wasserstein distances of chromatin cluster size distributions (left) and cluster number per cell distributions (right) for A549-H2B-GFP cells (in Supplementary Figure 6)

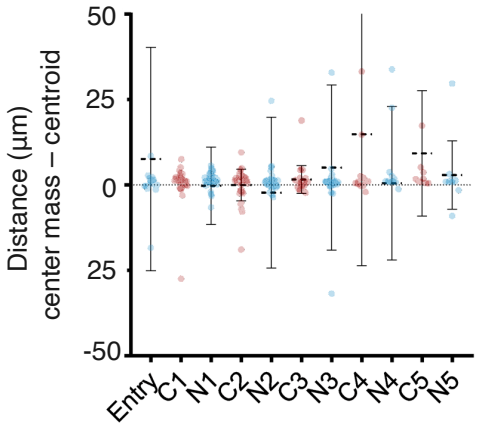

Supplementary Figure 8 Results for the potential location where chromatin clusters accumulate. Cell population analysis for the vertical distance between the intensity center of mass and the geometric center of the nucleus in PACA-H2B-GFP cells migrating through short channels (n=65). The center of mass represents the average position of fluorescence signal across all pixels. Positive distance values indicate that the intensity center of mass lies at the front of the cell (before the geometric center) while negative values indicate that it lies at the rear of the cell (after the geometric center). The distance from the center of mass to the geometric center along the microchannel direction is minimal and it does not exhibit a distinctive trend towards positive or negative values. Bars show mean ± standard deviation. Kruskal-Wallis test with Dunn's post hoc test for multiple comparisons was performed, p-value: $p<0.05$ (*), $p<0.01$ (**), $p<0.001$ (***).

Supplementary Note 1: Computational model for chromatin dynamics

Here we describe in detail the model introduced in Sec. 4.9 of the main manuscript. We express all magnitudes in terms of the basic units of length l_u, energy e_u and time t_u. Their equivalence to real units is explained in Appendix . Firstly, the chromatin fiber interlocking contiguous beads together is described by a harmonic potential[1, 2]

$$V_\mathrm{el} = \sum_{i=0}^{N-1} \frac{1}{2} k_\mathrm{el} (d_i - l_0)^2, \tag{1}$$

where $k_\mathrm{el} = 128 e_\mathrm{u}/l_\mathrm{u}^2$ is the elastic constant of the interaction, $d_i = |\mathbf{r}_{i+1} - \mathbf{r}_i|$ the distance between contiguous monomers i and $i+1$, $l_0 = l_\mathrm{u}$ the equilibrium distance between them and $\mathbf{r}_i$ the position vector with respect to the origin of the i-th particle. N is the total number of particles.

The rigidity of the chain is not considered in the model given the characteristic size of the coarse-grained nucleosomes, much larger than the typical persistence length (size of a domain considered rigid) of chromatin[3].

To account for both, the excluded volume effect (steric repulsion) of nucleosomes and the attraction between heterochromatic elements[4–6], Wang-Frenkel potential was considered[7],

$$V_\mathrm{W-F} = \sum_{i=0}^{N-1} \sum_{j=i+1}^{N} \varepsilon_\mathrm{cc} \left(\frac{\sigma^2}{d_{ij}^2} - 1 \right) \left(\frac{4\sigma^2}{d_{ij}^2} - 1 \right)^2 \tag{2}$$

where $\varepsilon_{cc} = 0.75 e_\mathrm{u}$ represents the depth of the potential well, serving as a modulator of the chromatin-chromatin interactions, $\sigma = l_\mathrm{u}$ is the effective radius of the nucleosomes and $d_{ij} = |\mathbf{r}_i - \mathbf{r}_j|$ the distance between monomers i and j.

In the case of steric interactions, the cutoff of the potential was taken at $d_\mathrm{steric} = 2\sigma/\sqrt{3}$ leading to a purely repulsive force. For heterochromatin-heterochromatin interactions, which also exhibit attractive behavior, cutoff was instead $d_\mathrm{het-het} = 2\sigma$. The potential is represented in Supplementary Figure 9b.

The heterochromatin elements of the chain can also interact with the lamina forming the nuclear envelop, although the results presented in Fig. 6 have this interaction turned off. In particular, heterochromatin elements may be attracted to any point forming the walls via another Wang-Frenkel potential,

$$V_\mathrm{wall} = \sum_{i=0}^{N} \varepsilon_\mathrm{cw} \left(\frac{\sigma^2}{d_{i,w}^2} - 1 \right) \left(\frac{4\sigma^2}{d_{i,w}^2} - 1 \right)^2 \tag{3}$$

where the interaction strength, when applicable, is $\varepsilon_\mathrm{cw} = 2.0 e_\mathrm{u}$ corresponds to the strength of the interaction with the walls, and $d_{i,w}$ represents the distance of the i-th bead to the closest wall element.

All these forces and potentials are integrated using the Langevin equation of motion. Given the size of the nucleosomes of the coarse grained model and the medium in which the dynamics occurs (later discussed), we neglected the inertial terms of the dynamics and integrated the equations of motion in the overdamped regime, as

$$\gamma \frac{d\mathbf{r}_i}{dt} = -\nabla_i V(\bar{r}) + c_0 \xi_i(t) \tag{4}$$

with $\gamma = e_\mathrm{u} t_\mathrm{u}/l_\mathrm{u}^2$ being the kinetic coefficient of the nucleosomes and $V = V_\mathrm{el} + V_\mathrm{ben} + V_\mathrm{W-F} + V_\mathrm{wall}$. The thermal noise is taken as gaussian white noise with zero mean $\langle \xi_i(t) \rangle = \mathbf{0}$ and delta correlated in time $\langle \xi_i(t) \xi_j(t') \rangle = \mathbf{I} \delta(t - t') \delta_{ij}$, with amplitude $c_0 = \sqrt{2\gamma k_B T}$, where k_B is the Boltzmann constant, T the temperature of the system, $\mathbf{I}$ is the identity second order tensor, and δ_{ij} is the Kronecker delta.

These equations were integrated using the 2$^\mathrm{nd}$ order Runge-Kutta[8, 9] with a timestep $\Delta t = 1/2048\ t_u$, and implemented in CUDA. This allowed for further optimization and parallelization of the dynamics, thus leading to larger chain sizes ($N \sim 60000$).

Coupled with the dynamics of the chromatin fiber is the change in geometry over time. The chain is confined within a lamina that shifts and transforms to reflect the evolution of the cell nucleus

observed in the experiments. The geometry (depicted in Supplementary Figure 9) is described in the transverse plane as the union of two circles of radius R_1 and R_2, whose centers are set at distances L_1 and L_2, respectively. The union is done via the use of two additional circles, tangent to them. The section joining the two initial circles thus forms the channel, whose thickness is kept at a width W proportional to the actual experimental setup ($W = 4\mu$m). This planar geometry is then extruded in the Z-axis for a total height of 6 μm.

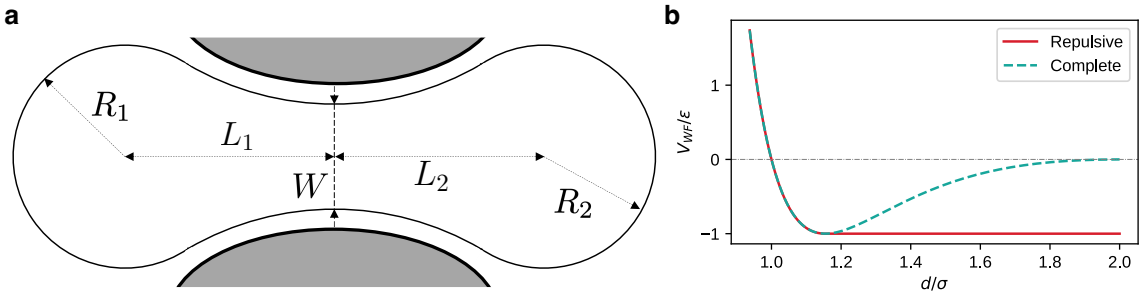

Supplementary Figure 9 **a** Schematic of the geometry for the confined cell projected on the transverse plane. The indents defining the constriction in the channel are colored in gray **b** Graphical representation of the W–F potential described in Eqs. (2) and (3). Both interaction types are shown: the complete potential (green dashed outline) and the purely repulsive form (solid red outline), truncated at $d/\sigma = 2/\sqrt{3}$.

The values of R_1, R_2, L_1 and L_2 are progressively varied during the simulation to emulate the evolution of the cell nucleus (more specifically, L_1 moves at a speed of approximately 0.41 μm/min towards the constriction and the other parameters are modified accordingly as to maintain the volume constant). Both the height and the area of the figure are kept constant, since changes in surface were of the order of 10% in the experimental setup. This restriction imposes a relation between the three variables. The initial condition of the system corresponds to $L_1 = L_2 = 0$ and $R_2 = 0$, i.e. a single circle on the left in the transverse plane. The chromatin occupies a fraction of $\rho \sim 0.2$ times the volume of the nucleus.

Simulation setup and thermalization

To choose an initial condition for the system, a chain of N monomers is progressively distributed semi-randomly (taking into account the connectivity of the chain) within the cylindrical cavity. Each particle is assigned as heterochromatin or euchromatin according to the distribution of the domains, exponential in nature and of average length of 128 monomers.

In order to solve any possible overlapping between monomers before the initial phase of the simulation, a soft repulsive potential is introduced during the initial stages of the simulation

$$V_{\text{soft}} = \sum_{i=0}^{N-1} \sum_{j=i+1}^{N-1} 128\,(d_{ij} + d_m/2)\,(d_{ij} - d_m)^2 \tag{5}$$

where $d_{steric} = (2/\sqrt{3})\sigma$ and $d_{ij} = |\mathbf{r}_i - \mathbf{r}_j|$ the distance between monomers i and j.

Afterwards, a short thermalization phase, followed by the production phase of the simulation, takes place.

Mapping model parameters to physical values

Within this section we will connect our relative magnitudes in terms of length, energy and time units to real values comparable to those seen experimentally. Firstly, the length unit σ corresponds to the radius of a chromatin bead. From coarse graining applied on our model, we obtain an average radius of $\sigma = l_{\text{u}}$.

As for the unit of energy, considering a DNA chain at room temperature conditions allows for the establishment of $e_{\text{u}} = k_{\text{B}}T = 4.11$ pN/nm.

For the time unit, we can calculate the value of the kinetic coefficient γ from Stokes' Law (assuming spherical isolated nucleosomes) as $\gamma = 6\pi\sigma\eta$, with $\eta = 2\eta_{\text{w}}$ being the viscosity of the medium, taken as two times that of water[10]. From there, the time unit $t_{\text{u}} = \gamma\sigma^2/k_{\text{B}}T \approx 8.06$ ms.

From these basic units all magnitudes can be reconstructed and translated into real values. Supplementary Table S1 summarizes some of the main parameters of the simulation, both in coarse-grained and physical units.

Parameter	Value (Dimensionless)	Value (Physical Units)
γ	$e_{\mathrm{u}} t_{\mathrm{u}} / l_{\mathrm{u}}^2$	$6\pi\eta\sigma = 2.12$ng /ms
$l_0 = \sigma$	l_{u}	125 nm
k_{el}	$128 e_{\mathrm{u}} / l_{\mathrm{u}}^2$	0.034 pN / nm
ε_{cc}	$0.75 e_u$	3.08 pN $\cdot$ nm
ε_{cw}	$2 e_u$	8.22 pN $\cdot$ nm
Δt	$(1/2048) t_u$	3.94 μs

Supplementary Table 1 Model parameter values both within the simulation setup and translated to real units.

The values of the constants ϵ_{cw} and ϵ_{cc} of the Wang-Frenkel interaction ($V_{\mathrm{W-F}}$) were chosen to qualitatively reproduce the experimental findings. As for the elastic coefficient of the chromatin fiber, k_{el}, we chose a value sufficiently large to provide relatively rigid bonds between chromatin beads.

Finally, and to justify the overdamped approximation taken for the integration of the equations of motion, Reynold's Number can be computed as $Re \approx 1.1 \cdot 10^{-6}$. This value corresponds to the regime in which inertial effects can be discarded, thus validating the overdamped conditions.

Additional results: different initial conditions.

Fig. 6 in the main manuscript contains one of the multiple simulations performed to study the dynamics of the chromatin fiber as it travels through the narrow channel. The results for different initial conditions of the system are shown in Supplementary Figure 10, equivalent to Fig. 6c.

The heatmaps show the same trend as in Fig. 6c, constriction during confinement leads to an increase in typical density values, i.e. condensation, which is partially reversed afterwards. The images thus demonstrate the reproducibility of the results, independent of initial condition, chromatin type distribution on the chain and random fluctuations due to temperature, thus supporting the conclusions drawn from the computational model in the main text.

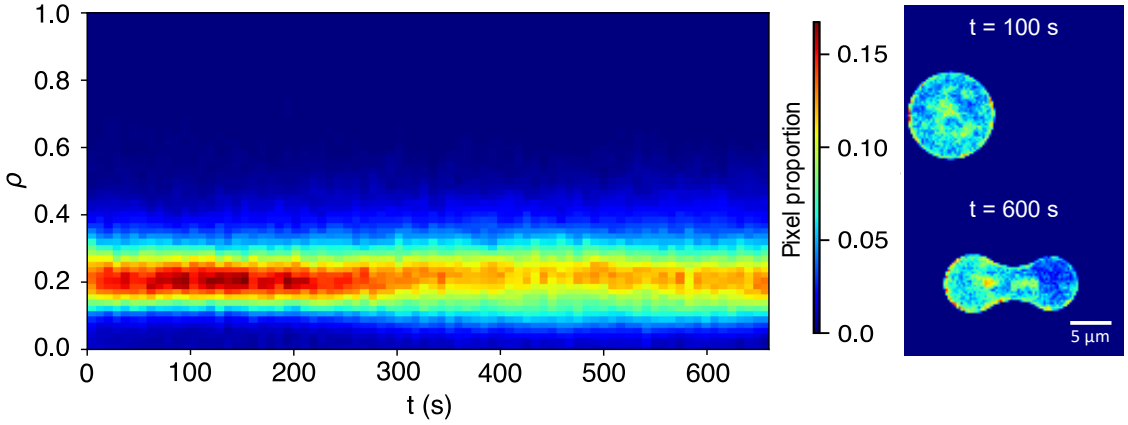

Supplementary Figure 10 Colormaps of the evolution over time (horizontal axis) of the distribution of chromatin density per pixel (vertical axis) for 4 different chromatin chains of $N = 60000$ and average domain size of 64 beads. The colors correspond to the amount of pixels with a particular chromatin density, with the color scale shown on the right. Each chain possesses different bead type (heterochromatin and euchromatin) distribution, as well as initial conditions in the simulation.

Additional results: comparison with other simulations

Simulations changing some of the parameters of the system were performed to analyze their individual effect on the results. In particular, one interesting modification by halving the average size of the typical domains of euchromatin and heterochromatin, from 64 to 32 beads. The results of the evolution of the chromatin concentration histograms can be found in Supplementary Figure 11.

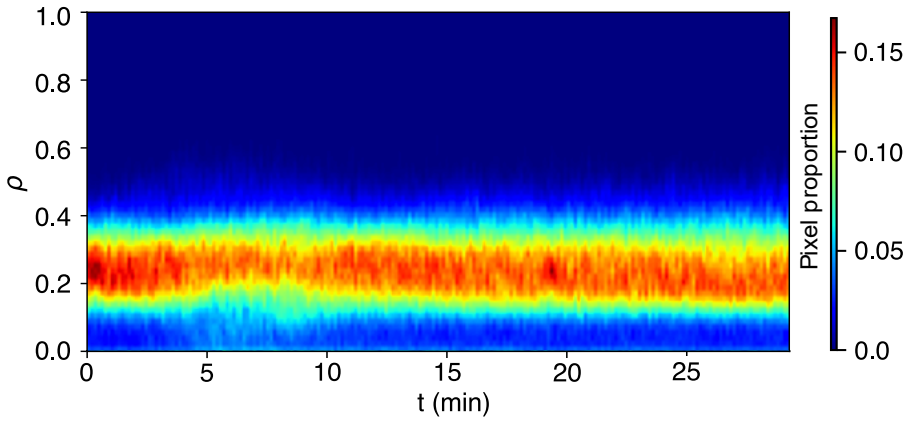

Supplementary Figure 11 Colormap of the evolution over time (horizontal axis) of the distribution of chromatin density per pixel (vertical axis) for a chromatin chain of $N = 60000$ and average domain size of 32 beads. The colors correspond to the amount of pixels with a particular chromatin density, with the color scale shown on the right.

A behavior similar to that of Fig. 6c is observed, with an increase in the width of the distribution after the beginning of the confinement (roughly 4 min), and shifting of the peak towards lower values of chromatin counts after traversing the confinement channel. However, the halved domain size leads to significantly smaller heterochromatin aggregates, thus making the results more difficult to observe in this figure.

Another interesting situation is the implementation of attractive interactions between the heterochromatin nucleosomes and the nuclear membrane walls, whose results are contained in Supplementary Figure 12.

Around the beginning of the confinement ($t \approx 5$ min), the width of the density distribution increases, similar to previous simulations, and returns to levels similar to those before traversing the narrow cavity once the system has exited confinement.

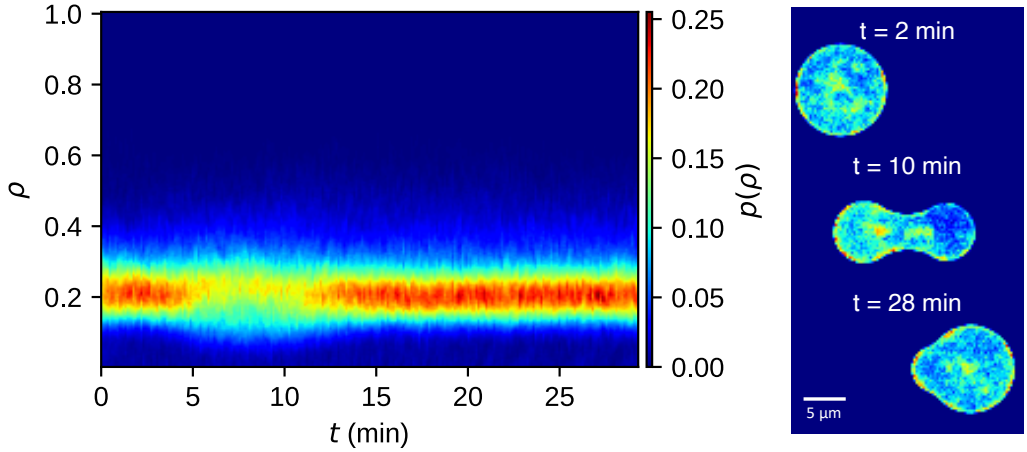

Supplementary Figure 12 On the left, colormap depicting the evolution over time (horizontal axis) of the histogram of chromatin amount per pixel (vertical axis) for a chromatin chain of $N = 60000$ and average domain size of 64 nucleosomes, with the wall-heterochromatin interaction turned on. The colors correspond to the amount of pixels with a particular chromatin count, with red colors representing higher counts. On the right, initial condition of the simulation (top, 2 min), intermediate configuration during confinement (middle, 10 min) and final conformation of the system (bottom, 28 min), displaying the spacial distribution of chromatin density.

However, notable differences with previous simulations appear when examining the spatial distribution of chromatin density at various times during the process (right panels of Supplementary Figure 12): from top to bottom, the initial state ($t = 2$ min), during confinement ($t = 10$ min), and after confinement ($t = 28$ min).

Already in the initial configuration, and unlike in simulations without wall attraction, a significant fraction of chromatin is located near the nuclear periphery, forming a distinct green outline corresponding to the envelope.

Upon constriction, the chromatin density distribution broadens, and this phenomena is accompanied by an increased accumulation of chromatin on the nuclear walls (see red pixels on the right of the middle panel of Supplementary Figure 12). As confinement advances, and because in this case the strength of the interaction with the walls (ϵ_{cw}) is higher than that of heterochromatin-heterochromatin interactions (ϵ_{cc}), those accumulations of chromatin on the confining walls remain attached, and grow over time. As a result, the final configuration exhibits most chromatin concentrated on the nuclear envelope, while the overall density profile returns to levels similar to those observed before constriction. The interactions with the walls seem to change the spatial distribution of chromatin, but not the global behavior of its density profile.

Supplementary References

[1] Bajpai, G. & Safran, S. Mesoscale, long-time mixing of chromosomes and its connection to polymer dynamics. *PLOS Computational Biology* **19**, 1–30 (2023).

[2] Amitai, A. & Holcman, D. Polymer physics of nuclear organization and function. *Physics Reports* **678**, 1–83 (2017).

[3] Bystricky, K., Heun, P., Gehlen, L., Langowski, J. & Gasser, S. M. Long-range compaction and flexibility of interphase chromatin in budding yeast analyzed by high-resolution imaging techniques. *Proceedings of the National Academy of Sciences* **101**, 16495–16500 (2004).

[4] Falk, M. *et al.* Heterochromatin drives compartmentalization of inverted and conventional nuclei. *Nature* **570**, 395–399 (2019).

[5] Adame-Arana, O., Bajpai, G., Lorber, D., Volk, T. & Safran, S. Regulation of chromatin microphase separation by binding of protein complexes. *eLife* **12**, e82983 (2023).

[6] Câmara, A. S. & Mascher, M. Consistencies and contradictions in different polymer models of chromatin architecture. *Computational and Structural Biotechnology Journal* **21**, 1084–1091 (2023).

[7] Wang, X., Ramírez-Hinestrosa, S., Dobnikar, J. & Frenkel, D. The lennard-jones potential: when (not) to use it. *Physical Chemistry Chemical Physics* **22**, 10624–10633 (2020).

[8] Greenside, H. & Helfand, E. Numerical integration of stochastic differential equations—ii. *Bell System Technical Journal* **60**, 1927–1940 (1981).

[9] Toral, R. & Colet, P. *Stochastic numerical methods: an introduction for students and scientists* (John Wiley & Sons, 2014).

[10] Luby-Phelps, K. Cytoarchitecture and physical properties of cytoplasm: volume, viscosity, diffusion, intracellular surface area. *International review of cytology* **192**, 189–221 (1999).